

Study of responsiveness of near-field terahertz imaging probes

Milan Berta, Petr Kužel and Filip Kadlec

Institute of Physics, Academy of Sciences of the Czech Republic, Na Slovance 2, CZ-182 21 Prague 8, Czech Republic

E-mail: kadlecf@fzu.cz

Received 21 April 2009, in final form 9 June 2009

Published 7 July 2009

Online at stacks.iop.org/JPhysD/42/155501

Abstract

We report on a study of the near-field sensitivity of a metal-dielectric near-field terahertz probe by time-domain terahertz spectroscopy. The obtained experimental data were analysed using principal component analysis. Principal components corresponding to the changes in the output terahertz pulse upon varying the probe-sample distance and reflecting the local anisotropy in a ferroelectric BaTiO₃ crystal were extracted and identified. Simulations of the pulse propagation within a model of the probe revealed very similar independent components.

(Some figures in this article are in colour only in the electronic version)

1. Introduction

In recent years, different terahertz (THz) and microwave imaging techniques have gained importance as promising tools for various applications [1–3], including imaging in pathological diagnosis [4–6], dentistry, tomography [7] and material inspection [8,9]. Many of these tasks can be accomplished using far-field imaging, though the spatial resolution is then limited by the wavelength used (300 μm at 1 THz), both in time-domain and continuous wave experiments. Near-field imaging techniques need to be employed to overcome this limitation and to resolve subwavelength features. The concept of THz spectral imaging with high spatial resolution offers the potential for investigation of objects with dimensions down to tens of nanometres [10]. Various approaches were developed with this aim, e.g. using transmission through a subwavelength aperture [11] or scattering from a metallic tip [12] placed near the surface of the investigated object [10]. These techniques commonly make use of a subwavelength structure which disturbs the electromagnetic field or limits its spatial distribution in the vicinity of the sample. The reflected or scattered radiation is detected and, as a result, a sensitivity to local sample properties is achieved. Consequently, only a small part of the incident radiation can be used to retrieve the near-field information. The tip-sample interaction in the time domain may be non-trivial and was recently the subject of other studies [13].

A broadband measurement method with a waveguiding pyramidal tip developed earlier [14] enables us to concentrate THz pulses into a small (subwavelength) volume at the tip end near the sample surface. However, the time-domain profile of the output THz pulses is influenced by the waveguide dispersion and by irregularities of the tip. Also, a rather small fraction of the output THz pulse reflected at the tip-sample interface carries the information about the sample local properties due to a high impedance mismatch between the partially metallized tip end and the adjacent sample medium. These features often prevent a straightforward evaluation of the raw experimental data.

Multi-dimensional data sets are usually generated during broadband THz imaging experiments using THz-TDS. Principal component analysis (PCA) [15] appears as one solution for decreasing the dimensionality of the time-domain THz data and for a simultaneous optimizing of their sensitivity with respect to the studied properties. Also, artificial feature definition and visualization of these features were proposed and applied successfully [16]. In this work, we use a variant of PCA [17,15] to identify principal components (PCs) in the detected field and their frequency distribution, which is a prerequisite for performing near-field imaging with spectral resolution. By using a simple linear transformation to reduce the dimensionality of the problem we are able to detect PCs linked to very weak changes in the frequency spectra. This enables us to evaluate the responsiveness of the

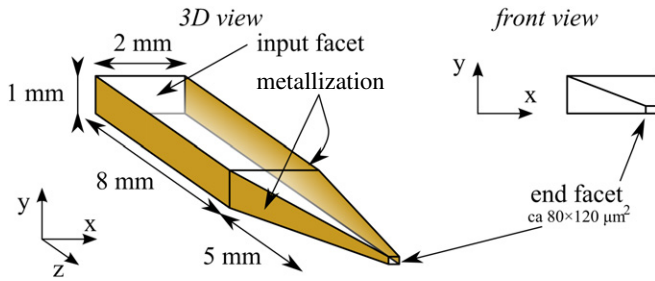


Figure 1. A schematic picture of an asymmetric sapphire probe with two neighbouring sides tapered and with metallization on two narrower sides.

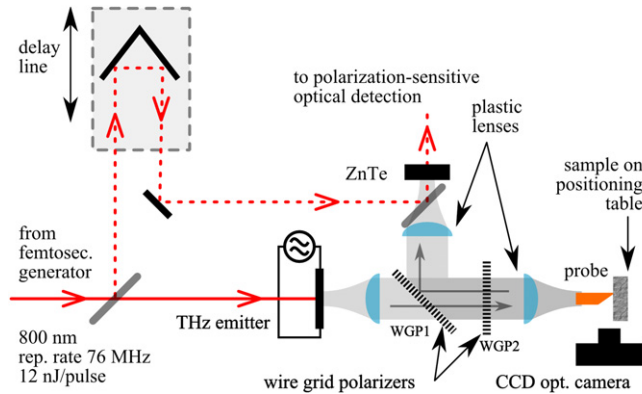


Figure 2. A schematic drawing of the THz near-field imaging setup. Optical pulses with an energy of 12 nJ (solid line) are converted to THz pulses (grey beam and arrows) at the emitter and a small fraction of these optical pulses (dashed line) deflected by a beam-splitter is used for electro-optic detection. The generated THz pulses are directed by plastic lenses and wire-grid polarizers onto the near-field probe.

method [14] with respect to spatial position, permittivity and local anisotropy of a sample.

2. Experimental setup

The measurement method is based on a near-field probe which consists of a rectangular-shaped block of a low-loss dielectric material (sapphire was used in our case) sharpened to an asymmetric pyramidal tip terminated by a subwavelength-sized plane facet, see figure 1. Two opposite sides of the probe were metallized—the coating consisted of a 10 nm titanium adhesive layer, 1 μm of silver and 30 nm of gold as a protective layer. The dimensions of the end facets of our probes were in the range from 80×120 to $90 \times 140 \mu\text{m}^2$. The tapering focuses the incident wave onto the end facet, giving rise to a highly localized electromagnetic field. This field is thus sensitive to the permittivity (conductivity) in the close vicinity of the end facet and it is suitable for broadband applications [14].

The frequency range 0.1–1.4 THz was investigated in a setup for the time-domain THz spectroscopy. A schematic drawing of the setup is shown in figure 2. Free-space propagating THz pulses are generated using Ti:sapphire 50 fs long laser pulses and a Tera-SED large-area biased

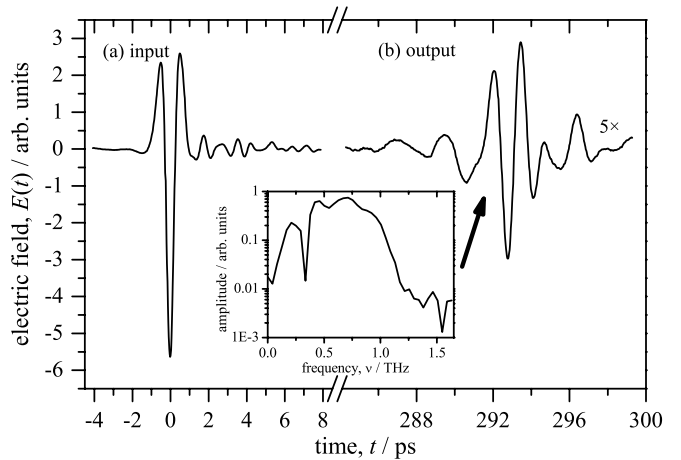


Figure 3. A typical THz waveform from the input facet of the probe (a) and profile of the THz pulse reflected off the tip, multiplied by 5 (b). The strong after-ringing in the input waveform is due to absorption by water vapour. The mean frequency of the output pulse frequency range (inset) was evaluated to $\nu_m \approx 0.60$ THz.

photoconductive emitter [18]. The THz pulses are focused by a pair of plastic lenses onto the input facet of the probe so that the polarization of the radiation is perpendicular to the metallized surface of the probe. The radiation travels along the probe and the focusing in the pyramidal part is enabled by the metallization on two opposite sides. In this way, the electromagnetic field is guided and concentrated around the end facet. The focused field pattern interacts with the close environment of the tip, and a substantial part of the radiation is reflected back. These back-reflected pulses are directed by the wire-grid polarizers and plastic lenses onto a 1 mm thick ZnTe crystal. The orientation of the wire-grid polarizers is such that it is possible to deflect the back-reflected pulses to the detection system: the first polarizer (WGP1) is oriented along the polarization of the incident THz radiation, while the second one (WGP2) is turned by $\pi/4$ against the first one. The temporal profiles of the electric intensity of the THz pulses $E(t)$, also called waveforms, are detected by means of electro-optic sampling [19] in the ZnTe crystal. Typical examples of an incident THz pulse (input waveform) and of a back-reflected pulse from the tip (output waveform) are shown in figure 3. Different materials placed into the proximity of the tip leave different fingerprints in the shape of the output waveforms.

Although the concept of the probe is simple, it was experienced that small deviations in the adjustment of the probe with respect to the incident THz beam, irregularities in its geometry caused by fabrication (mainly the shape of the end facet), and also dynamic perturbations like air density fluctuations in the free-air THz beam path, influence the shape of the reflected pulses. Changes in the waveforms caused by the dynamic deviations are often comparable to the level of the useful signal. It therefore appears difficult to extract the information relevant to the sample properties without applying a mathematical post-processing method on the experimental data.

3. Data analysis and simulations

PCA is a kind of linear transformation which was applied to analyse the raw experimental data obtained at different experimental configurations and to separate the PCs corresponding to experimental parameters. This multivariate method [17] was used to reduce the dimensionality of the problem. The R environment [20] for statistical computing was used to decompose the data by singular value decomposition. A set of experimentally obtained waveforms $E(t, \alpha)$ were collected where α is a parameter varied in the experiment. The decomposition is aimed at identifying the influence of the parameter α on the measurements or, possibly, also at increasing the experimental sensitivity with respect to this parameter. First, the Fourier transform is calculated for each of the waveforms to obtain spectra $E(\nu)$; then the data matrix is written as a sum of N PCs [17, 21]:

$$E(\nu, \alpha) = \sum_{j=1}^N C_j A_j(\alpha) f_j(\nu); \quad (1)$$

here only the amplitudes of the spectra $E(\nu)$ are taken into consideration. The j th independent PC is factorized and consists of a product of three terms: a weight coefficient C_j and the normalized amplitudes $A_j(\alpha)$ and $f_j(\nu)$. The total number of the PCs, N , is equal to the number of the experimental values of the parameter α . The PCs are ordered in decreasing order: $C_{j+1} \leq C_j$. The first PC ($j = 1$, the component with C_1 and amplitudes $A_1(\alpha)$ and $f_1(\nu)$) is the main component and is very close to the average of the spectra. Only components up to a certain index j have physical meaning. The scree test [22] was used to select the significant components and to reject the so-called noise components—those creating the noise floor. An example of the applied scree test is in the inset of figure 4.

The behaviour of the output spectrum was analysed at three measurement configurations. First, the performance of the experiment was characterized in a situation when no sample was present in front of the tip and no additional changes during the experiments were made. The analysis of this first configuration revealed PCs originating from time-varying disturbances, such as thermal oscillations (within 1 °C) and air flow irregularities. Thus, it was possible to identify these PCs in further experiments and configurations.

In the second experimental configuration, we placed a single-domain BaTiO₃ sample close to the $80 \times 120 \mu\text{m}^2$ end facet of the sapphire probe. We then varied the tip-sample distance d and PCA characterization of the output waveforms of the near-field pattern was accomplished. The PCA revealed distance dependences of various PCs; their examples are depicted in figure 4. Apart from the main PC ($j = 1$), four other significant PCs can be distinguished. All of them appear to exhibit universal behaviour which was also observed when other tips were used. The amplitudes of the PCs with $j > 2$ extend up to $d \sim 100 \mu\text{m}$, while the second PC vanishes much earlier. Further, with the growing j , the number of oscillations over the measured distance for all $A_j(d)$ increases, too.

PCA of simulations obtained by using CST MicroWave Studio@2008 software tool [23] also revealed several PCs

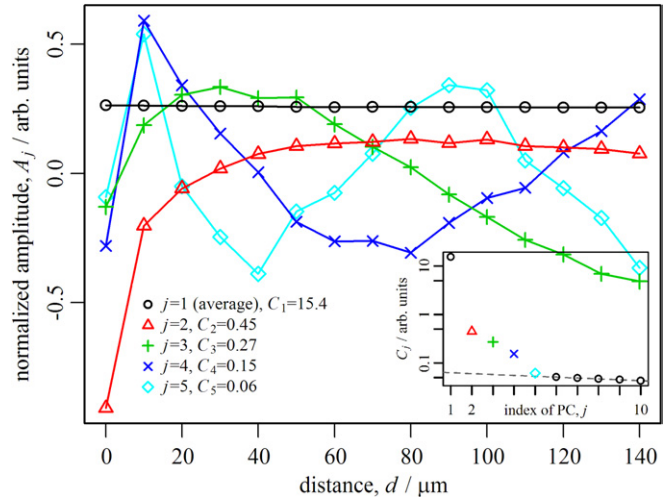


Figure 4. Characteristic examples of amplitudes $A_j(d)$ of the experimentally obtained output THz pulse depending upon the tip-sample distance d , for $j \leq 5$. Inset: example of a scree test for determining the noise floor.

depending on the tip-sample distance. A model of a shorter probe with a $50 \times 100 \mu\text{m}^2$ end facet was created and fed with a Gaussian excitation pulse in the frequency range 10–300 GHz. This lower frequency range was required by the software tool capabilities with respect to model proportions and extended meshing. The distance d between the tip and the sample (with a permittivity $\epsilon = 56$) was then varied across an interval of $100 \mu\text{m}$ with a step of $4 \mu\text{m}$. The output pulses yielded by the simulations were analysed by PCA and five significant PCs were identified; for comparison with the amplitudes $A_j(d)$ extracted from the experiment, see figure 5. The abscissae were rescaled to d/ν_m , where the mean frequency ν_m takes on the values of 0.155 THz and 0.60 THz in the case of simulations and for the experimental data, respectively. The ratio d/ν_m seems to represent a scale-invariant quantity which would be independent of the frequency range of the incident pulse. The explanation of this form of rescaling does not seem to be straightforward, and it is still a subject of our investigation. However, in this particular case, its validity appears justified in view of the similarity of the amplitude curves after rescaling, see figure 5. One can see that despite the different frequency ranges and the shapes of the input and output pulses, the simulations and the experiments give similar results with respect to the extracted amplitudes $A_j(d)$. Higher-order PCs with lower C_j were observed; however, in simulations, they are affected by the changing meshing conditions as d was varied, and they constitute the noise floor. The number of steps made in the vicinity of the sample is low due to a limitation of the meshing density and the computational time, but it is sufficient for comparing the results of simulations with the experimental data, see figure 5. We can observe that there is a good overall agreement between amplitude dependences $A_j(d)$ extracted from the simulations and from the experiments.

Finally, it was demonstrated that the output THz pulses exhibit features related to the anisotropy of the probed samples. To check the sensitivity of the tip to the anisotropy of a sample, sample-orientation dependent measurements were

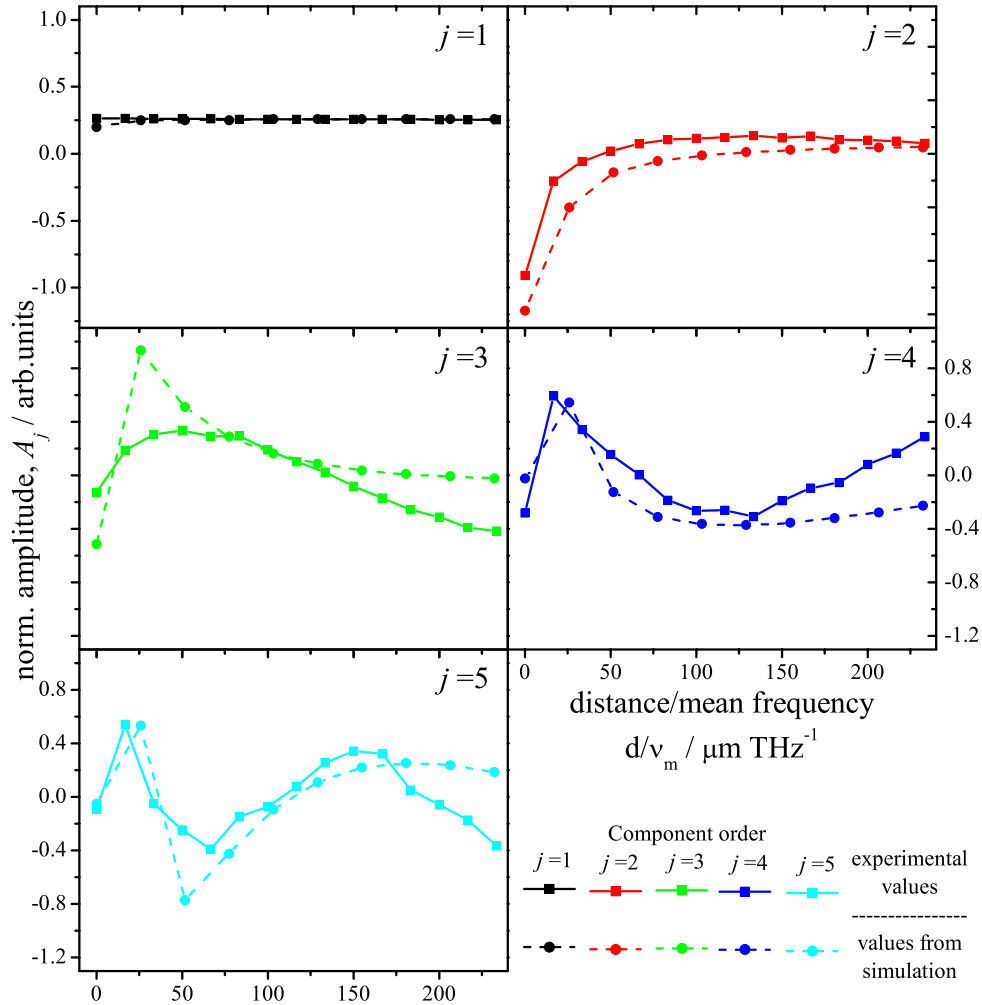


Figure 5. Comparison of the amplitudes $A_j(d)$ extracted from the experimental and the simulated data sets. The amplitudes are plotted against the ratio d/v_m , where d is the distance between the sample and the end facet of the probe and v_m is the mean frequency of the frequency range of the output pulse.

performed. In this third configuration, a flat as-grown BaTiO₃ single-domain crystal platelet was used, which exhibits a high anisotropy; its refractive indices are $n_o = 45$, $n_e = 7.5$ in the THz and microwave frequency ranges [24]. The sample surface was placed in touch with the probe, perpendicular to its axis and rotated around this axis by an angle φ . The output waveforms were recorded at each orientation. Analysis of the data revealed a PC which is orientation dependent. A sinusoidal fit of the amplitude of this PC ($j = 3$) is shown in figure 6. The response is π -periodical which means that this component reflects chiefly the sample anisotropy itself and it is not related to other raw measurement errors due to, e.g. tilted sample surface. The PC with $j = 2$ showed an uncorrelated behaviour and was assigned to air density fluctuations. Finally, PCs of $j = 4$ and $j = 5$ showed a 2π -periodical behaviour which is probably due to a small misorientation between the sample normal and the probe axis.

4. Discussion

The presented results illustrate the typical performance of the employed near-field THz time-domain imaging method.

While time-dependent perturbations of the measurement apparatus are undesirable, they can be difficult to avoid and they will manifest themselves, to some extent, in the experimental data. Furthermore, although a substantial part of the generated THz radiation is propagating through the imaging probe near the location where the sample is placed, only a small part of it, corresponding to the evanescent field, depends on the presence and properties of the sample. Employing the PCA appears to be an efficient approach for identifying the small individual contributions to the experimentally obtained waveforms, namely the parts of the signal due to deliberately varied parameters, systematic and random errors (i.e. instability of experimental setup and noise, respectively).

The dependence of the PCs on the probe–sample distance d shows unexpected behaviour. In the observed tip–sample distance window of $140 \mu\text{m}$, the amplitudes $A_j(d)$ display a number of oscillations (no oscillation for $A_1(d)$, one oscillation for $A_2(d)$, and so on); they become denser in d as their order j increases. This result was not only obtained from the experimental data but also confirmed by our computer simulations. The good agreement between the

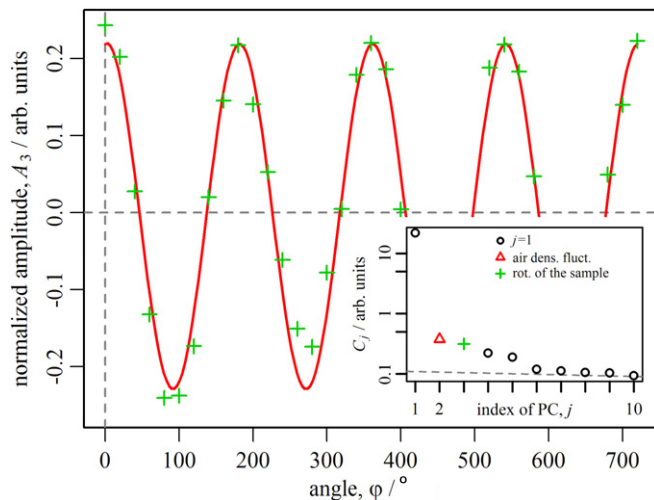


Figure 6. A sinusoidal fit (solid line) to the amplitude $A_3(\varphi)$ (symbols) describing the angular dependence of the output THz pulses when BaTiO₃ sample was turned by $2 \times 360^\circ$ (4π). Inset: scree test showing the five significant PCs.

shapes of the $A_j(d)$ amplitudes obtained from experiments and simulations shows clearly that this distribution of amplitudes is a property of the near-field probe itself, and it is not significantly influenced by its deviations from ideal shape and electromagnetic characteristics. The second PC $A_2(d)$ appears to have a decay similar to what was shown in recent absorption measurements using a microstrip-line near-field THz waveguiding technique [25]. In that work, the evanescent electric field above THz on-chip waveguides was used to measure dielectric samples.

Also, we observe that it is difficult to find a correlation among amplitudes in frequency $f_j(\nu)$ in a given set of measurements. In view of this observation, it appears that one can gain information about the complex space and frequency distribution of the field at the end facet of the probe, but imaging of a sample surface with a spectral resolution seems a hard task using this experimental technique.

The results evidencing the sensitivity of the near-field probe with respect to local anisotropy are, to our knowledge, the first of this kind. Although the amplitude $A_3(\varphi)$ is not much higher than the components corresponding to the noise floor in the experiment, we show that it is possible to distinguish the orientation of the BaTiO₃ crystallographic axes from the output waveforms. This observation also brings the method a step closer to imaging applications with high spatial resolution where the contrast among various parts of the samples is lower than that between a metal and a common dielectric. Thus, imaging of ferroelectric domains at the scale of tens of micrometres should become feasible with convenient samples and probe tip dimensions.

5. Conclusion

We have presented experimental results obtained with our metal-dielectric near-field probe. These results were further processed using PCA and components sensitive to the sample dielectric properties and to the distance between the sample

and the probe were identified. The frequency dependence of these components is yet unpredictable and this can be a substantial obstacle for performing spectroscopy connected with two-dimensional imaging employing this technique. To improve the sensitivity of the experimental setup, we have also distinguished and subtracted components originating from systematic and random errors. The electromagnetic field localized in the vicinity of the probe tip is well polarized, therefore characterization of local anisotropy is also possible. We have investigated a highly anisotropic BaTiO₃ crystal and demonstrated that the probe is sensitive to the orientation of its domains. The study thus suggests that the probe is potentially useful for visualization of orientation of ferroelectric domains with a spatial resolution of tens of micrometres.

Acknowledgment

The authors would like to acknowledge financial support by the Ministry of Education of the Czech Republic (project LC-512), Grant agency of the Charles University (project 113-10/259209) and by the Czech Academy of Sciences (project AVOZ 10100520).

References

- [1] Mittleman D (ed) 2004 *Sensing with Terahertz Radiation* 1 edn Berlin: (Springer)
- [2] Fitzgerald A J, Berry E, Zinovev N N, Walker G C, Smith M A and Chamberlain J M 2002 An introduction to medical imaging with coherent terahertz frequency radiation *Phys. Med. Biol.* **47** R67–84
- [3] Chan W L, Deibel J and Mittleman D M 2007 Imaging with terahertz radiation *Rep. Prog. Phys.* **70** 1325–79
- [4] Wallace V P, Fitzgerald A J, Shankar S, Flanagan N, Pye R, Cluff J and Arnone D D 2004 Dermatological surgery and lasers: terahertz pulsed imaging of basal cell carcinoma *ex vivo* and *in vivo* *Brit. J. Dermatol.* **151** 424–32
- [5] Pickwell E and Wallace V P 2006 Biomedical applications of terahertz technology *J. Phys. D: Appl. Phys.* **39** R301–10
- [6] Nakajima S, Hoshina H, Yamashita M and Otani C 2007 Terahertz imaging diagnostics of cancer tissues with a chemometrics technique *Appl. Phys. Lett.* **90** 041102
- [7] Withayachumnankul W et al 2007 T-ray sensing and imaging *Proc. IEEE* **95** 1528–58
- [8] Zhang X-C 2004 Three-dimensional terahertz wave imaging *Phil. Trans. R. Soc. Lond. A* **362** 283–99
- [9] Dean P, Shaikat M U, Khanna S P, Chakraborty S, Lachab M, Burnett A, Davies G and Linfield E H 2008 Absorption-sensitive diffuse reflection imaging of concealed powders using a terahertz quantum cascade laser *Opt. Express* **16** 5997–6007
- [10] Huber A J, Keilmann F, Wittborn J, Aizpurua J and Hillenbrand R 2008 Terahertz near-field nanoscopy of mobile carriers in single semiconductor nanodevices *Nano Lett.* **8** 3766–70
- [11] Chen Q, Jiang Z, Xu G X and Zhang X-C 2000 Near-field terahertz imaging with a dynamic aperture *Opt. Lett.* **25** 1122–4
- [12] Cho G C, Chen H-T, Kraatz S, Karpowicz N and Kersting R 2005 Apertureless terahertz near-field microscopy *Semicond. Sci. Technol.* **20** S286–92
- [13] Thoma A and Dekorsy T 2008 Influence of tip-sample interaction in a time-domain terahertz scattering near field scanning microscope *Appl. Phys. Lett.* **92** 251103

- [14] Klein N, Lahl P, Poppe U, Kadlec F and Kužel P 2005 A metal-dielectric antenna for terahertz near-field imaging *J. Appl. Phys.* **98** 014910
- [15] Pei J, Hu Y and Xie W 2007 PCA-Based visualization of terahertz time-domain spectroscopy image *Proc. SPIE* **6787** 67871M
- [16] Löffler T, Siebert K, Czasch S, Bauer T and Roskos H G 2002 Visualization and classification in biomedical terahertz pulsed imaging *Phys. Med. Biol.* **47** 3847–52
- [17] Martens H and Næs T 1991 *Multivariate Calibration* (New York: Wiley)
- [18] Dreyhaupt A, Winnerl S, Dekorsy T and Helm M 2005 High-intensity terahertz radiation from a microstructured large-area photoconductor *Appl. Phys. Lett.* **86** 121114
- [19] Nahata A, Auston D H, Heinz T F and Wu C 1996 Coherent detection of freely propagating terahertz radiation by electro-optic sampling *Appl. Phys. Lett.* **68** 150–2
- [20] R Development Core Team 2008 R: A language and environment for statistical computing <http://www.R-project.org>
- [21] Sharma S 1995 *Applied Multivariate Techniques* (New York: Wiley)
- [22] Cattell R B 1966 The scree test for the number of factors *Multivariate Behav. Res.* **1** 245–76
- [23] CST 2008 CST MicroWave studio@ <http://www.cst.com/>
- [24] Li Z, Grimsditch M, Foster C M and Chan S-K 1996 Dielectric and elastic properties of ferroelectric materials at elevated temperature *J. Phys. Chem. Solids* **57** 1433–8
- [25] Byrne M B, Cunningham J, Tych K, Burnett A D, Stringer M R, Wood C D, Dazhang L, Lachab M, Linfield E H and Davies A G 2008 Terahertz vibrational absorption spectroscopy using microstrip-line waveguides *Appl. Phys. Lett.* **93** 182904